

High-pressure cycling of hematite α -Fe₂O₃: Nanostructuring, *in situ* electronic transport, and possible charge disproportionation

Sergey V. Ovsyannikov,^{1,2,*} Natalia V. Morozova,³ Alexander E. Karkin,⁴ and Vladimir V. Shchennikov³¹*Bayerisches Geoinstitut, Universität Bayreuth, Universitätsstrasse 30, Bayreuth D-95447, Germany*²*Institute for Solid State Chemistry of Russian Academy of Sciences, Urals Division, 91 Pervomayskaya Str., Yekaterinburg 620990, Russia*³*High Pressure Group, Institute of Metal Physics of Russian Academy of Sciences, Urals Division, GSP-170, 18 S. Kovalevskaya Str., Yekaterinburg 620990, Russia*⁴*Research Department on Nuclear Reactor; Institute of Metal Physics of Russian Academy of Sciences, Urals Division, GSP-170, 18 S. Kovalevskaya Str., Yekaterinburg 620990, Russia*

(Received 9 January 2012; revised manuscript received 22 October 2012; published 30 November 2012)

We studied electronic transport properties of hematite (α -Fe₂O₃) at room temperature under cycling of high pressure up to ~ 22 GPa. The original samples and those recovered after high-pressure experiments were examined by x-ray diffraction and Raman and optical absorption spectroscopy. At ambient pressure the original samples were also characterized by temperature measurements of electrical and galvanomagnetic properties. Upon compression, the original single crystals underwent a sluggish structural deconfinement starting above 5 GPa into a nanometric state. Above 5–7 GPa, the nanostructured hematite showed a reversible transition to a state with enhanced electrical conductivity and moderate values of thermoelectric power (Seebeck effect) of about $-150 \mu\text{V/K}$. This electronic phase corresponds to neither conventional trivalent oxidation state of the iron ions in hematite nor metallic conductivity. Analysis of the electronic transport data in the frameworks of two models, of polaron hopping, and of intrinsic semiconductor conductivity, revealed a change from the electron conductivity to two-band electrical conductivity and suggested that the observed enhancement of the electrical properties in nanocrystalline α -Fe₂O₃ above 5–7 GPa is related to the mixed-valence state of the iron ions. Since α -Fe₂O₃ is believed to undergo a “spin-flop” (Morin) transition near 2–5 GPa at room temperature, we discuss potential contributions of magnetoelastic and other effects to the observed high-pressure properties of hematite.

DOI: [10.1103/PhysRevB.86.205131](https://doi.org/10.1103/PhysRevB.86.205131)

PACS number(s): 72.20.Pa, 73.61.Ey, 71.22.+i, 61.50.Ks

I. INTRODUCTION

Iron oxides, Fe_xO_y, are composed of two the most abundant elements in the Earth, and these materials are crucially important for basic and applied sciences, as well as for industry. The iron oxides are represented by Fe₂O₃, Fe₃O₄, FeO, and Fe₄O₅; the last oxide has been recently synthesized in high-pressure-high-temperature conditions.¹ The valence state of Fe ions has a major influence on properties of Fe_xO_y systems. In particular, their electronic transport may be described in the framework of the model of small-polaron conductivity—charge exchange between Fe²⁺ and Fe³⁺ ions,^{3,4} and hence, the Fe³⁺/Fe²⁺ ratio is a key parameter. Besides structural transformations, an applied pressure can induce intriguing electronic/magnetic crossovers, e.g., near 5–10 GPa in FeO,^{4,5} and 6–15 GPa in Fe₃O₄.^{3,6} However, the nature of these features is still a point at issue.

At ambient conditions, Fe₂O₃ normally adopts a corundum lattice (α -Fe₂O₃, space group #167, $R\bar{3}c$). Undoped hematite with an optical band gap of ~ 1.8 – 2.3 eV,^{7–9} shows very low electrical conductivity. However, intrinsic conductivity may be enhanced by annealing in reducing conditions, which leads to the appearance of oxygen vacancies and related Fe²⁺ ions.^{2,8,10} Polaron conductivity models tightly bind the Fe³⁺/Fe²⁺ ratio to a thermopower value.^{2–4} Intrinsic α -Fe₂O₃ was therefore suggested to be a sensitive “thermoelectric gas sensor” of oxygen partial pressure.¹¹

At temperatures near $T_M \sim 255$ K, hematite exhibits a “spin-flop” (so-called Morin) transition.¹⁰ At this transition, the spins below T_M are reoriented from being aligned

perpendicular to the c axis to be aligned parallel to the c axis.¹⁰ This leads to changes in magnetic (from ferromagnetic to antiferromagnetic)^{10,12} and elastic properties (bulk modulus reduces by $\sim 10\%$).^{13,14} Pressure–temperature boundaries of the Morin transition seem to be very sensitive to sample mesostructure and pressure conditions. Thus, in nanocrystalline samples, the transition temperature (T_M) drops below 160 K, and a hysteresis loop between the direct and return transitions significantly extends.^{15,16} Even the shape of hematite particles can affect the course of the Morin transition and T_M .¹⁷ Additionally, in nanostructured samples, this transition was found to be accompanied by dramatic changes in magnetic properties, which stimulated speculation about the possible existence of new intermediate magnetic and structural phases.¹⁸ With pressure application, T_M rises and reaches room temperature at ~ 2 – 5 GPa, as found by variation of magnetic^{19–23} and elastic properties.^{13,14} A high-pressure neutron diffraction study suggested stabilization of an “intermediate” orientation of the spins above ~ 2.5 – 3 GPa.²⁰ However, hitherto electrical resistivity studies of α -Fe₂O₃ under pressure could not detect any effect of this spin-flop transition on the electronic band structure of α -Fe₂O₃.²⁴

In this work, we examine the electronic transport in α -Fe₂O₃ crystals under pressure cycling up to 22 GPa (i.e., across the spin-flop transition). This treatment led to nanostructuring of the samples. We find evidence of a mixed-valence state of the iron ions in nanostructured hematite compressed above 5–7 GPa.

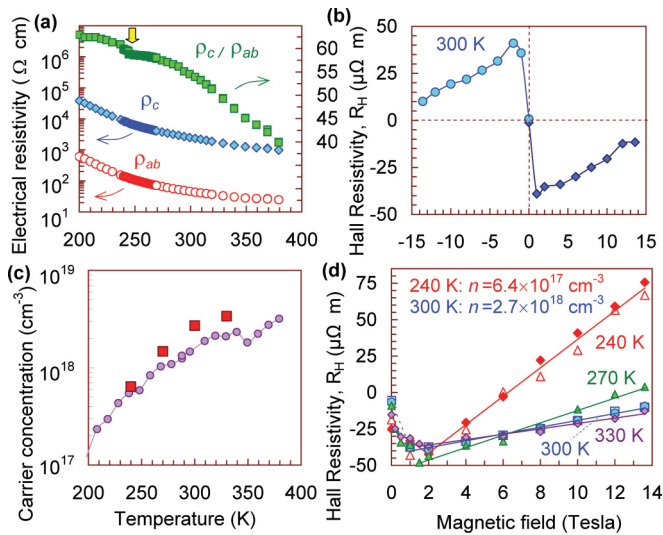


FIG. 1. (Color online) Temperature dependencies of (a) electrical resistivities along the ab or c axis, and of (c) carrier concentration, and (b, d) magnetic field dependencies of the Hall resistivity of α - Fe_2O_3 . (a) The bulk arrow indicates the Morin transition. (b) Separation of normal and anomalous (below 1 T) Hall effects [see Eq. (1)]. (c) Big squares, concentrations determined from the normal Hall effects in plot (d); small points, rough estimations from full Hall signal at 13.6 T. (d) Determination of carrier concentration from the normal Hall effect at several temperatures, for both increasing and decreasing values of the magnetic field.

II. DETAILS OF EXPERIMENT

In this work, we used chemically pure quasi-single-crystalline ingots of hematite (α - Fe_2O_3). At ambient pressure the original samples were also characterized by temperature measurements of electrical and galvanomagnetic properties carried out by a conventional Montgomery method (a modification of a Van der Pauw method) using an Oxford Instruments setup (Fig. 1),²⁵ covering a range of temperatures from 200 to 380 K and of magnetic fields up to 13.6 T.

The high-pressure experiments were carried out in anvil-type high-pressure cells [Figs. 2(a) and 2(b)], loaded in an automated high-pressure setup (minipress), connected with nanovoltmeters and a computer.²⁶ This automated setup smoothly generated a force applied to a high-pressure cell and automatically registered the electrical signals from a sample and environment for both pressurization and decompression cycles.²⁶ A force applied to a high-pressure cell was measured by means of a digital dynamometer with resistive-strain sensors. Pressure values were estimated from a calibration curve based on the well-known and distinctly observable pressure-induced transitions with a possible uncertainty in the maximal pressure value below $\sim 10\%$.²⁶

The high-pressure anvils made of synthetic diamonds had culets of ~ 600 – $1000 \mu\text{m}$ in diameter (Fig. 2).²⁷ A microscopic plate-shaped sample $\sim 200 \mu\text{m}$ in diameter and $\sim 30 \mu\text{m}$ thick was loaded in a container made of lithographic stone (soft CaCO_3 -based material) [Fig. 2(c)]. This container served both as a gasket and a pressure-transmitting medium [Fig. 2(c)].²⁷ The Seebeck effect was measured by the conventional method

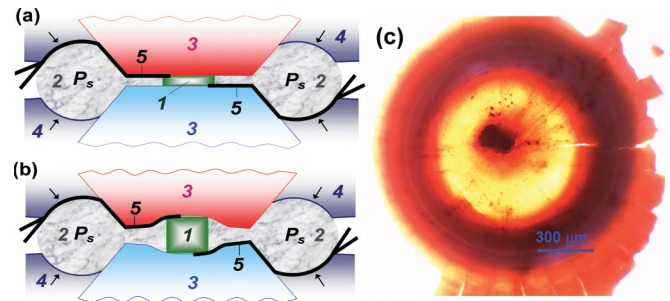


FIG. 2. (Color online) Side views of high-pressure cell with (a) conventional “flat” and (b) concave “toroidal” anvils, and (c) photograph of a container with a sample (black rectangle in the center) recovered after high-pressure cycling experiments. 1, sample; 2, container made of the lithographic stone; 3, anvils (in thermoelectric measurements, the upper anvil is heated—shown in red); 4, supporting hard-alloy matrices made of tungsten carbide; 5, electrical probes to a sample. A ringlike bulge of container 2 provides a supporting pressure P_s (up to 10 GPa) around the tips of the anvils; high, quasihydrostatic pressure P is being created in the central part of the container around a sample.

by generating a temperature difference (ΔT) between two edges of a sample and measurement of a thermoelectric voltage between these edges.²⁸ We generated this ΔT along a sample thickness by electrical heating the upper anvil [Figs. 2(a) and 2(b)].²⁶ A ΔT value was determined from a temperature difference between the upper and lower anvils, which was directly measured by means of the thermocouples.^{26,29} A (thermo-)electrical signal from a sample was measured by thin Pt-Ag electrical probes. In order to monitor changes in the electrical conductivity characteristics of the samples under pressure cycling, we measured electrical resistance (Fig. 3) from the same Pt-Ag electrical probes with a quasi-four-probe technique (two bifurcated wires) [Figs. 2(a) and 2(b)]. Since the wide-band-gap α - Fe_2O_3 had low electrical conductivity, the conductivity of microscopic parts of the high-conductive Pt-Ag electrical probes could not affect the measurements.

The merits of the thermopower method we employed in this study were as follows: (i) a uniform thermal flow went exclusively through the sample bulk from the upper “hot” to the lower “cold” anvil [Figs. 2(a) and 2(b)], and (ii) the lithographic stone container provided good thermal isolation for a sample. We measured the Seebeck effect in three regimes as follows: (i) at a fixed pressure value under gradual variation in ΔT (Fig. 4); (ii) at a fixed ΔT under gradual variation in pressure [Fig. 5(a)]; and (iii) at simultaneous variations in both pressure and ΔT . All three methods gave identical results. We carried out comparative studies on several samples cut from the same ingot of α - Fe_2O_3 for several pressure cycles up to ~ 17 – 22 GPa.

Before and after the pressure experiments, the samples were examined by x-ray diffraction (XRD) and Raman and optical absorption spectroscopy studies (Figs. 6–8). The XRD studies were performed using an in-house high-brilliance Rigaku diffractometer (wavelength, $\lambda = 0.7108 \text{ \AA}$) equipped with Osmic focusing x-ray optics and a Bruker Apex CCD detector. The Raman spectra were excited with red and green

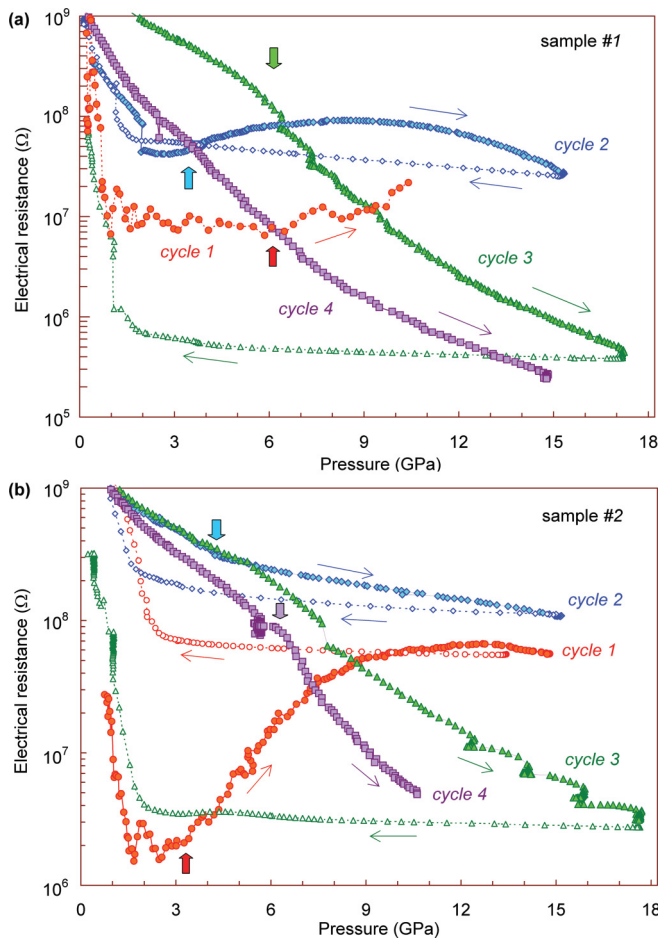


FIG. 3. (Color online) Electrical resistance dependencies of two α -Fe₂O₃ samples (a) 1 and (b) 2 under high-pressure cycling at 295 K. The pressure cycle numbers are given near the curves. The thin arrows show the direction of pressure variation. The bulk arrows indicate characteristic kinks in the curves.

laser lines and were recorded in a backscattering geometry. The spectra excited with the red 632.8-nm line of a He-Ne laser were recorded using a LabRam spectrometer, whereas the spectra excited with the green 514.5 nm line of an Ar laser were recorded using a T64000 Jobin–Yvon triple grating monochromator. The Raman signal from the hematite samples was rather strong, and the high-quality spectra were collected for 5–20 minutes. Optical absorption spectra were recorded using a Bruker IFS 120 Fourier-transform spectrometer coupled to an all-reflecting Bruker microscope. The original single-crystalline sample was polished from both sides to a thickness of $\sim 15 \mu\text{m}$. The samples recovered after the high-pressure experiments had a similar thickness and flat surfaces. The absorption spectra were measured in a range of 8000–25 000 cm^{-1} ($1 \text{ eV} \approx 8065 \text{ cm}^{-1}$) by use of a tungsten source, a Si-coated CaF₂ beam splitter, and a narrowband mercury-cadmium-telluride detector. Each spectrum was obtained by averaging over two spectra, each consisting of 200 scans. The spot size on the sample was varied from 30 to 350 μm to make sure of the absence of noticeable edge effects. Other details may be found in previous works.³⁰

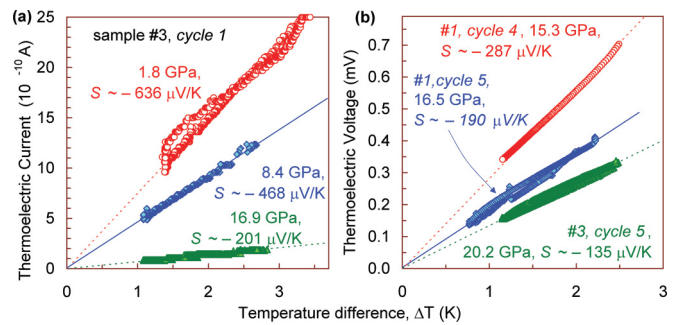


FIG. 4. (Color online) Examples of determination of Seebeck effect from linear slopes of dependencies of (a) thermoelectric current and (b) thermoelectric voltage on a temperature difference along a sample, ΔT . (a) Plot shows data collected on the first pressurization cycle of sample 3. (b) Plot shows data collected at samples 1 and 3. Most of the curves combine increasing and decreasing ΔT cycles.

III. RESULTS AND DISCUSSION

Single-crystalline hematite samples show a tiny jump in conductivity ratio, ρ_c/ρ_{ab} , at $\sim 250 \text{ K}$ [Fig. 1(a)] that could be attributed to the Morin transition.¹⁰ From the $\rho(T)$ curves [Fig. 1(a)] we estimated an activation energy as of $E_a = 0.14 \text{ eV}$. Like Fe₃O₄,²⁵ α -Fe₂O₃ exhibits both normal and anomalous Hall effects [Fig. 1(b)]; hence, Hall resistivity, ρ_H , is summed as²⁵

$$\rho_H = R_N B + R_A \mu_0 M, \quad (1)$$

where, R_N (R_A) is the normal (anomalous) Hall coefficient, μ_0 is magnetic susceptibility, and M is magnetization. Hence, R_N is determined from a linear slope of a $\rho_H(B)$ curve after magnetization has saturated (i.e., $> 1 - 2 \text{ T}$) [Figs. 1(b) and 1(d)]. Following this procedure, we determined the electron concentrations, n , at several temperatures [Fig. 1(d)]. From these $n(T)$ data points, we found a bit lower activation energy of $E_n \approx 0.13 \text{ eV}$. Using the known expression, $\mu = 1/(e \times n \times \rho_{ab})$ (where, e is the electron charge) we established a carrier mobility value at 300 K as of $\sim 0.05 \text{ cm}^2/(\text{B} \times \text{c})$, in agreement with previous reports.¹⁰ Notice that previous studies documented that mobility also has an activation character.¹⁰

In general, the electrical and thermoelectric studies under pressure were carried out on three samples of hematite cut from the same ingot and labeled 1, 2, and 3. Samples 1 and 2 were examined by the electrical resistance technique to monitor changes in the electrical conductivity characteristics under pressure cycling (Fig. 3). Direct measurements of thermopower under pressure were possible when the sample resistance became low enough. We performed thermopower studies starting from the decompression runs of the fourth cycle both on samples 1 and 2 (Figs. 4 and 5). Sample 3 was examined by combined thermopower and electrical resistance studies (Figs. 4, 5, and 9). We could not verify sample orientation before the transport measurements.

One can see that the pressure dependencies of the electrical resistance, $R(P)$, measured on samples 1 and 2 strongly vary with pressure cycle (Fig. 3). These resistivity data (Fig. 3) correlate with the discrepancies in previous high-pressure resistivity studies of α -Fe₂O₃.²⁴ On the first cycle, the $R(P)$ curve of sample 2 showed a decrease in the resistance value up

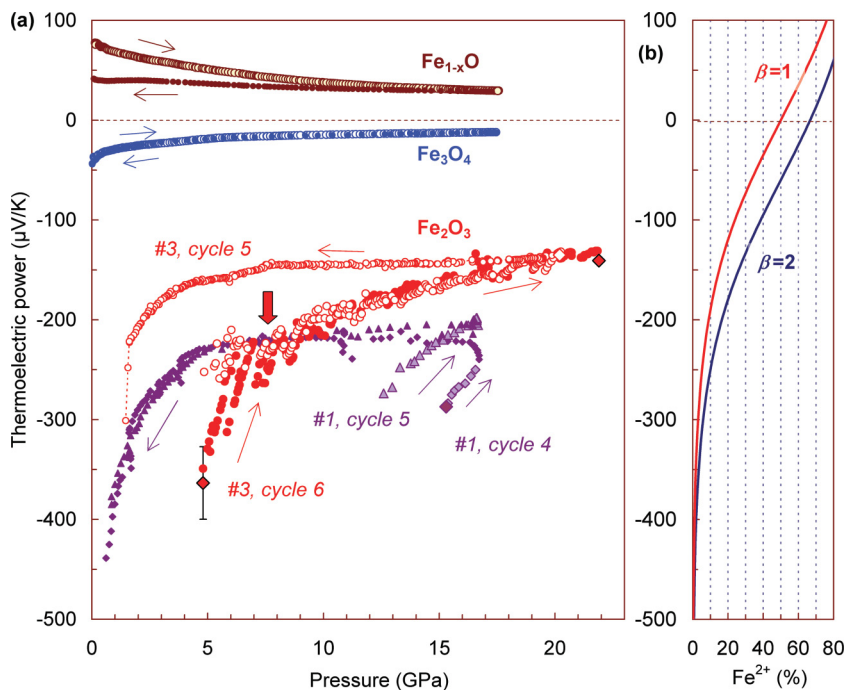


FIG. 5. (Color online) (a) Pressure dependencies of thermoelectric power (Seebeck effect) for two samples, 1 and 3, of α - Fe_2O_3 at 295 K. Typical thermopower curves of Fe_3O_4 (from Ref. 3) and Fe_{1-x}O (from Ref. 4) are shown for comparison. The notations are the same as in Fig. 3. Several of the larger symbols correspond to values found from the linear slopes of dependencies of thermoelectric voltage on a temperature difference along a sample (like those shown in Fig. 4). (b) Dependencies of thermopower (ordinate) on $\text{Fe}^{2+}/(\text{Fe}^{2+} + \text{Fe}^{3+})$ ratio, calculated by Eq. (3) for $\beta = 1$ and 2.

to ~ 1.5 –3 GPa, and then a gradual rise to a flat maximum near 13 GPa (Fig. 3). The successive pressure cycles demonstrated a gradual lowering of resistance with pressure, with a kink down above 5–7 GPa [Fig. 3(b)]. In the first cycle, sample 1 was compressed only up to ~ 10 GPa, and this could explain the difference in the second cycles between samples 1 and 2 [Fig. 3(a)]. Although, in this case, we can also notice a tendency of resistance to growth on the first pressure cycle above ~ 6 GPa [Fig. 3(a)]. Near ambient conditions, the thermopower values in our samples were $S \sim -(500\text{--}1000) \mu\text{V/K}$, as expected for intrinsic stoichiometric α - Fe_2O_3 .^{2,10,11,31} Direct thermopower measurements performed on the fourth and further pressure cycles found values of $S \sim -(130\text{--}250) \mu\text{V/K}$ at 15–22 GPa [Fig. 5(a)]. Upon decompression, the thermopower returned to values below $-400 \mu\text{V/K}$ [Fig. 5(a)]. Notice, that *in situ* thermoelectric measurements under pressure remain challenging, and so far there were no reports on α - Fe_2O_3 . As seen from Figs. 3 and 5(a), the pressure-driven changes in the transport properties look to some extent reversible.

All the samples recovered after pressure cycling to 17–22 GPa exhibited pronounced signatures of nanostructuring, as seen from XRD and Raman studies (Figs. 6–8). The original, shiny, single-crystalline samples deconfined into bulk nanometric samples that could readily crumble to reddish nanoparticle dust (Fig. 6). The unit cell parameters in the recovered samples were similar to those in the original crystal [$a = 5.033(2) \text{ \AA}$ and $c = 13.747(4) \text{ \AA}$]. The Rietveld refinement of the XRD patterns of the recovered samples (Fig. 6) could propose only a minor shift in the oxygen x coordinate. To estimate an average size of nanograins in the recovered samples by the XRD data, we applied the well-known Williamson–Hall method of separation of grain and strain effects, as follows:³²

$$\{\beta_{\text{obs}} - \beta_{\text{inst}}\} \cos \theta = \lambda/D_V + 4\varepsilon_{\text{str}}\{\sin \theta\}, \quad (2)$$

where β_{obs} and β_{inst} are the observed and instrumental integrated breadths (in radians 2θ) of a reflection located at 2θ , respectively; D_V is the volume-weighted crystallite size; and ε_{str} is the weighted average strain. To account for instrumental resolution, in the same conditions, we measured the XRD of a commercial microcrystalline powder of α - Fe_2O_3 and used this pattern as a reference. Using Fullprof software, we refined the XRD patterns of the recovered samples (Fig. 6) and determined averaged reflection breadths (Fig. 7). Following the Williamson–Hall method in Eq. (2), we estimated average size of crystallites as $D_V \sim 10\text{--}20$ nm (e.g., $D_V \sim 15\text{--}17$ nm [12–13 nm] in sample 1 [3]) (Fig. 7). It should be also stressed that compression itself may not be a reason for nanostructuring. For instance, metastable Fe_{1-x}O subjected to the same pressure cycling up to 20 GPa did not show that.⁴

In order to determine conditions of hematite nanostructuring, we investigated two more samples and verified that a multicycle pressure treatment up to only 5 GPa (sample 4) does not lead to nanostructuring [Figs. 6(c) and 7(c)], but one pressure cycle up to 17 GPa (sample 5) does lead to nanostructuring ($D_V \sim 15$ nm) [Figs. 6(f) and 7(d)]. Taking into account the apparent difference in second-cycle behavior between samples 1 and 2 (Fig. 3), we can conclude that structural deconfinement is a sluggish process that happens between 5 and 17 GPa. Therefore, the second and further pressure cycles (Figs. 3–5) show property changes in nanostructured hematite. The first-cycle $R(P)$ curve of sample 2 should reflect changes related to the deconfinement process (Fig. 3). After the electrical resistance of sample 2 reaches the maximum near 13 GPa, its further behavior resembles that of the second-cycle curve [Fig. 3(b)]; hence, it seems that the process is nearly completed at 13 GPa. Sample 1 in the second pressure cycle shows rather similar behavior [Fig. 3(a)]. Variations in the behavior of electrical resistance on further pressure cycles (Fig. 3) correlate with very strong dependence of the Morin transition temperature, T_M on nanocrystallite size.¹⁵ Gradual growth in the electrical

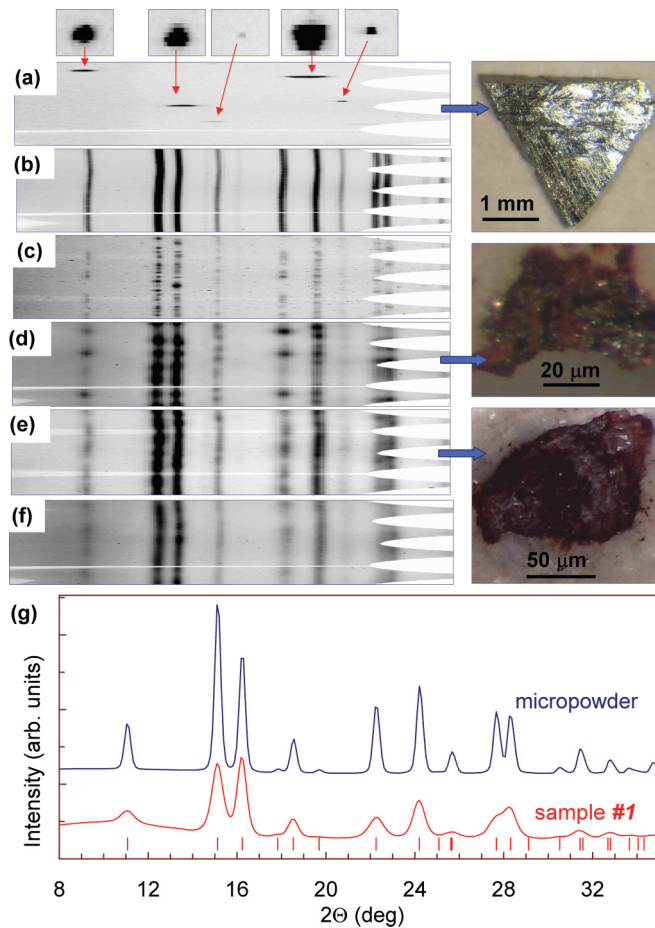


FIG. 6. (Color online) X-ray diffraction (XRD) patterns and photographs of the original and recovered samples of α -Fe₂O₃ after high-pressure experiments at 295 K. (a–f) Examples of azimuth XRD images in the full range of 0–360°. (g) Examples of integrated 2D XRD patterns. (a) The large single crystal of α -Fe₂O₃. The ordinate azimuth axis has been strongly shrunk to assemble XRD images of several samples inside one figure. Five small upper insets show the spotlike single-crystal diffraction reflections in a regular scale. (b) Commercial microcrystalline powder of α -Fe₂O₃ ($D_V > 100$ nm). (c) Sample 4 recovered after multicycle pressure experiments up to ~ 5 GPa. (d) Sample 1 recovered after multicycle pressure experiments up to 17 GPa [Fig. 3(a)]. (e) Sample 3 recovered after multicycle pressure experiments up to 22 GPa [Figs. 5(a), 9(a), and 9(b)]. (f) Sample 5 recovered after the one-cycle run-up to 17 GPa. To improve the quality of the XRD patterns, some samples were slowly rotated during data acquisition. The photographs of the original and a couple of the recovered samples are given at the right side of the figure. (g) The tick marks are calculated peak positions for the corundum lattice. The widening of the XRD peaks of the samples recovered after the high-pressure experiments suggests their nanostructuring. Typical average sizes of the nanograins are estimated in Fig. 7.

resistance value is a characteristic feature of a structural disordering process that affects the scattering of charge carriers. It has been shown on example of silicon that structural deconfinement leads to enhancement of nanoplasticity as “nanoparticles are less constrained and display dislocation-driven plasticity.”³³ Well-documented compression curves of hematite show that its plastic deformation begins

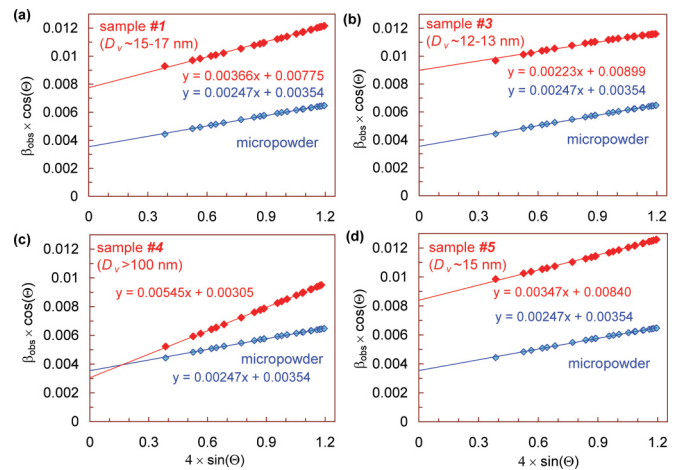


FIG. 7. (Color online) Williamson–Hall plots for four α -Fe₂O₃ samples recovered from high-pressure experiments after the multicycle experiments up to 17 GPa (a, sample 1), up to 22 GPa (b, sample 3), and up to 5 GPa (c, sample 4) and after the one-cycle run-up to 17 GPa (d, sample 5). Microcrystalline powder ($D_V > 100$ nm) was used as a reference material, which permitted estimation and accounting for an experimental instrumental widening of the diffraction peaks.

above ~ 4 –6 GPa,¹⁴ a single-crystal study up to 5 GPa did not detect that.³⁴

Nonhydrostatic pressure effects should favor structural deconfinement. It is interesting to notice that nonequilibrium and nonhydrostatic shock-wave treatment up to ~ 8 –27 GPa was already revealed to be an effective method of nanometric hematite preparation.¹⁶ A very recent neutron diffraction study has also demonstrated that a slight deviation from pressure hydrostaticity above the Morin transition leads to nanostructuring.²³ In addition, this study has detected the reappearance of the main magnetic (003) reflection that should not be observable beyond the spin-flop transition.²³ On the contrary, on very slow and perfectly hydrostatic pressurization of a hardened sample, potentially one can avoid sample nanostructuring beyond the above critical pressures.³⁵ This particular behavior of hematite under moderate pressures is probably the main source of discrepancies in the phase-transition scenarios and properties at higher pressures documented in different studies.^{24,36}

Nanostructuring of bulk materials under pressure is possible in the course of reconstructive phase transitions that are accompanied by significant volumetric changes (e.g., GaN).³⁷ At room temperature above 30–60 GPa, hematite transforms to a Rh₂O₃(II)-type phase with metal-like conductivity, but its behavior under higher pressures remains a point at issue.^{24,36} Compression in nonhydrostatic conditions did not lead to any noticeable downward shift in the transition pressure.³⁸ Nanometric hematite that was prepared during a pressure-driven phase transition from nanometric maghemite (γ -phase of Fe₂O₃ having a spinel crystal structure with vacancies at the iron sites) also did not exhibit any transformation up to 30 GPa.³⁹ Thus, no structural phase transitions could occur in our samples upon compression up to 17–22 GPa. Our electronic transport data (Figs. 3–5) apparently do not correspond to a metal-like conductivity found in the Rh₂O₃(II)-type

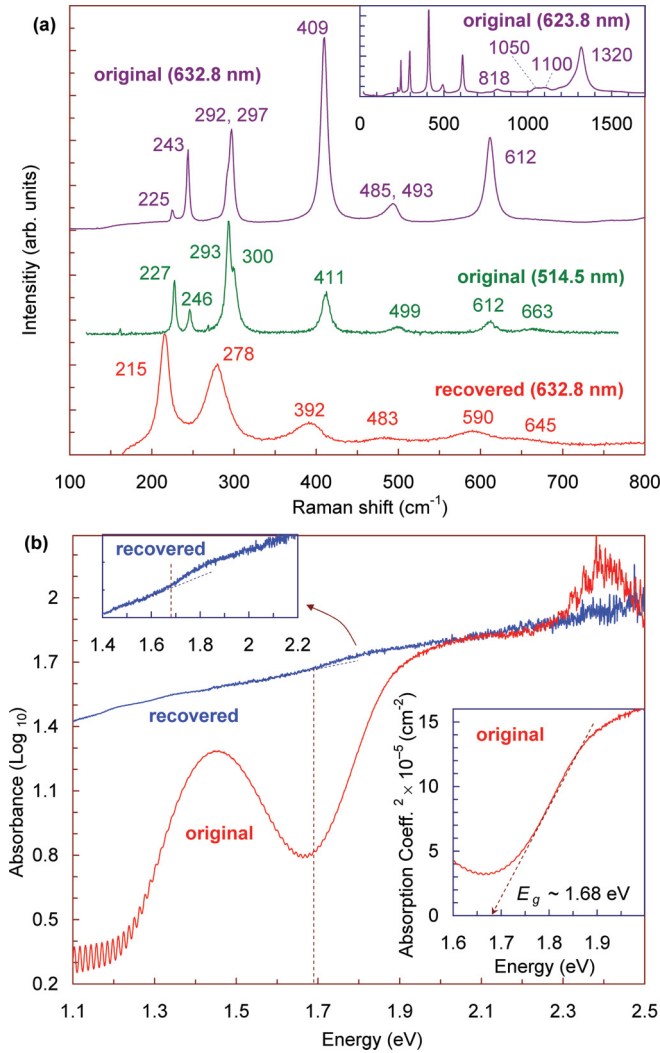


FIG. 8. (Color online) (a) Raman and (b) optical absorption spectra of the original and recovered sample 1 of α -Fe₂O₃ after high pressure at 295 K. (a) The inset shows a full Raman spectrum of the original crystal. (b) The x axis units were converted from [cm⁻¹] into [eV] (8065 cm⁻¹ = 1 eV). The upper inset shows the absorption edge in the recovered sample. The lower inset shows determination of the optical band gap in the original sample in the direct-gap model.

phase.²⁴ Therefore, we can supposedly link the structural deconfinement in hematite to the strong magnetoelastic effects that emerge in the course of the magnetic spin-flop transition.^{13,14,16,23} Nanostructuring in the course of a magnetic transition seems to be a unique case requiring further investigation and is beyond the scope of the present work.

In bulk α -Fe₂O₃, the beginning of the spin-flop transition at room temperature was seen at 2–3 GPa.^{13,14,19,20} Therefore, the minimum in the first-cycle $R(P)$ curve of sample 2 near 1.5–3 GPa [Fig. 3(b)] could be related to the beginning of this transition. However, at ambient pressure, the spin-flop transition in bulk α -Fe₂O₃ is accompanied by only very minor changes in electronic transport properties [Fig. 1(a)]^{2,31,40} and does not lead to structural deconfinement. This fact hints that the nature of the pressure-driven magnetic transition may be different (to some extent), as was proposed earlier.²⁰ Here, we notice a correlation with documented nonequivalence

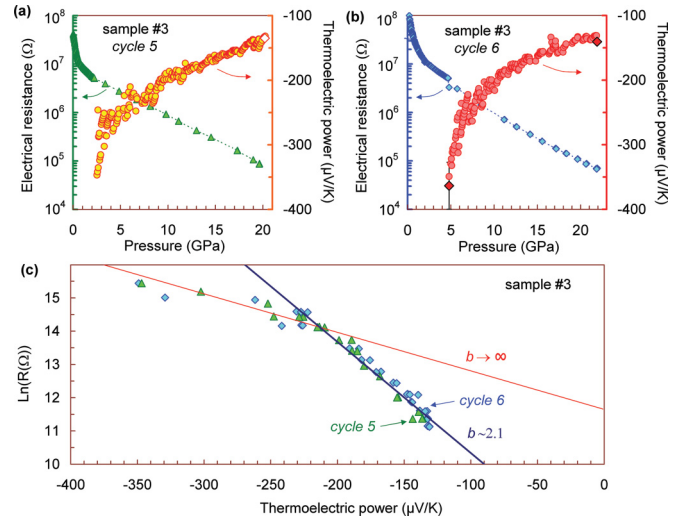


FIG. 9. (Color online) Determination of the ratio of electronic to hole conductivity ($b = \sigma_n/\sigma_p$) in α -Fe₂O₃ under pressure at 295 K. Upper plots show pressure dependencies of the electrical resistance and thermoelectric power of sample 3 measured simultaneously at fifth (a) and sixth (b) cycles, respectively. The thermopower data were already partly presented in Fig. 5(a). (c) A parametric dependence of “electrical resistance vs thermopower” constructed by the data presented in panels (a) and (b). This curve points a kink near -215 μ V/K and suggests the ratio $b = \sigma_n/\sigma_p$ to be ~ 2.1 above ~ 7 GPa.

of temperature- and pressure-driven “insulator-metal”-type transitions in similar oxides, V₂O₃ and Ti₂O₃.⁴¹ In addition, in nanocrystalline samples, some new features might emerge (e.g., superparamagnetism in nanograins).⁴² As mentioned above, in nanometric samples, T_M drops dramatically (which would suggest an upward shift in transition pressures), and the transition hysteresis loop extends;¹⁵ these two facts have a good correspondence with our findings (Fig. 3).

The Raman [Fig. 8(a)] and optical absorption [Fig. 8(b)] spectra of the original and recovered samples corroborate a strong disordering in the latter, in agreement with the XRD data (Fig. 6). The Raman spectra of the recovered samples demonstrated a pronounced softening of the phonon frequencies [Fig. 8(a)], in line with earlier reported spectra of nanocrystalline α -Fe₂O₃.⁴³ The optical absorption spectra of the original crystals exhibited an exciton at ~ 1.45 eV and an absorption edge at higher energies [Fig. 8(b)]. It has been established that the electronic band structure of α -Fe₂O₃ has an extremum in the valence band and almost parallel lower edge of the conductance band, suggesting a (nearly) direct band gap.⁹ A linear absorption edge in our samples also indicated that. Using the well-known expression, $\alpha = \alpha_0[(E - E_g)/E_g]^n + C$ (where α is the absorption coefficient, α_0 is a constant, E is energy, C is an instrumental shift, and $n \sim 1/2$ for direct gaps), we find a band-gap value of $E_g = 1.68$ eV [Fig. 8(b)]. This value is a bit lower than previous estimations, $E_g \sim 1.8$ – 2.3 eV.^{7–9} The nanostructured sample 1 with $D_V \sim 15$ – 17 nm [Fig. 7(a)] recovered after the high-pressure experiments exhibited traces of the absorption edge at nearly the same energy [Fig. 8(b)]. This agrees with

reports documenting a band-gap widening for nanocrystallites with D_V less than ~ 8 nm only.⁴³

The decrease in R and $|S|$ in nanostructured hematite with pressure (Figs. 3–5, and 9) clearly indicates an enhancement of conductivity. For thermopower data analysis, we employed models of small polaron hopping [Eq. (3)]^{2–4} and of intrinsic semiconductor [Eq. (4)],²⁸ as follows:

$$S = -\frac{k}{|e|} \ln \left(\beta \frac{\text{Fe}^{3+}}{\text{Fe}^{2+}} \right), \quad (3)$$

$$S = -\frac{k}{|e|} \left[\frac{b-1}{b+1} \times \frac{E_g}{2kT} + \left(r_n + \frac{5}{2} \right) \frac{b}{b+1} - \left(r_p + \frac{5}{2} \right) \frac{1}{b+1} - \frac{3}{4} \ln \frac{m_p^*}{m_n^*} \right], \quad (4)$$

where E_g is the band gap, k is Boltzmann's constant, e is the electron charge, β is the degeneracy factor including both spin and orbital degeneracy of electron carriers (typically $1 \leq \beta \leq 2$), $b = \sigma_n/\sigma_p$ is a ratio of partial conductivities of electrons and holes, and $r_n(r_p)$ and $m_n^*(m_p^*)$ are the scattering parameter and the effective mass of electrons (holes), respectively.

The electrical conductivity mechanism in α -Fe₂O₃ may be described in terms of polaron hopping between the Fe²⁺ and Fe³⁺ ions, located in crystallographically equivalent sites.² This hopping in the basal ab plane was calculated to have a low activation barrier of ~ 0.11 – 0.14 eV.² Using Eq. (3) for sample 1 at 15 GPa, we can roughly estimate Fe²⁺/Fe³⁺ as ~ 0.1 and ~ 0.2 for $\beta = 1$ and 2, respectively (Fig. 5). Likewise, for sample 3 at 22 GPa, Fe²⁺/Fe³⁺ ~ 0.25 and 0.43 for $\beta = 1$ and 2, respectively (Fig. 5). Such a “mixed-valence” state in stoichiometric hematite might be formed due to charge disproportionation of a group of the Fe³⁺ ions (i.e., $2\text{Fe}^{3+} \rightarrow \text{Fe}^{4+} + \text{Fe}^{2+}$). At normal conditions, this charge disproportionation in α -Fe₂O₃ is known to have a very high energy barrier of ~ 2 eV,⁴⁰ and likely for this reason, we did not observe it in bulk or partially nanocrystalline α -Fe₂O₃ in this work. Hence, one can surmise that the density of grain boundaries would play a key role in this process. This supposition agrees with our observations: sample 3, having average nanocrystallite sizes of $D_V \sim 12$ – 13 nm, exhibits the lower $|S|$ values and the higher Fe²⁺/Fe³⁺ ratios (Fig. 5) than sample 1 with $D_V \sim 15$ – 17 nm (Figs. 6 and 7). The mechanism of such a charge disproportionation in nanostructured material is not obvious and requires further extensive investigations. We can propose that in the course of the magnetic transition, the activation barrier for the charge disproportionation is greatly reduced for the Fe³⁺ ions located at or near the grain boundaries (i.e., in the less constrained areas). It is worth mentioning that some ferrites are known to show charge disproportionation under pressure [e.g., $2\text{Fe}^{4+} \rightarrow \text{Fe}^{3+} + \text{Fe}^{5+}$ in CaFeO₃ and (Sr,Lu)FeO₃].⁴⁴ Potentially, the Fe⁴⁺ ions could also contribute a bit to the charge transfer process in hematite. A very recent discovery of signatures of exotic “trimerisation” (Fe³⁺-Fe²⁺-Fe³⁺) in the charge ordering of another iron oxide, Fe₃O₄ below the Verwey transition at ~ 120 K,⁴⁵ hints that the charge redistribution in nanostructured hematite potentially might be tricky as well. Our findings have a good correlation with those of a very recent study of electrical properties of bulk and nanocrystalline maghemite (γ -Fe₂O₃) powders probed by means of impedance spectroscopy under pressures of up

to ~ 30 GPa.⁴⁶ This study separately investigated pressure evolution of “grain” and “grain boundary” resistivities and found that the latter dramatically decreased with pressure in nanocrystalline maghemite and became immeasurably small above 7.4 GPa;⁴⁶ however, bulk maghemite powder did not show such effects.⁴⁶

Expressing an “effective” E_g in Eq. (4) via electrical resistivity $\rho = \rho_0 \exp[E_g/(2kT)]$ (where E_g is the band gap and k is Boltzmann's constant),²⁸ one can find a relation between S and ρ as follows: $S \approx -(k/e)[(b-1)/(b+1)] (\ln \rho - \ln \rho_0)$. Since pressure dependence of ρ_0 is much weaker than ρ , the former could be neglected. This approach permits direct determination of the $b = \sigma_n/\sigma_p$ ratio from the “ ρ vs S ” parametric curve. On the fifth and sixth pressure cycles of sample 3, we carried out simultaneous measurements of electrical resistance and thermopower under pressure [Figs. 9(a) and 9(b)] and constructed such an “ R vs S ” dependence [Fig. 9(c)]. This curve shows an apparent slope change near $-215 \mu\text{V/K}$ that corresponds to ~ 7 GPa (Fig. 9). Thus, above ~ 7 GPa, the $b = \sigma_n/\sigma_p$ ratio in sample 3 may be estimated as ~ 2.1 . Therefore, the electrical conductivity in hematite changed from pure electron to a mixed p - n conductivity with $\sigma_n/\sigma_p \sim 2.1$ (Fig. 9). This estimation correlates with the above findings from the polaron hopping model Eq. (3) for sample 3 (Fig. 5).

IV. CONCLUSION

In this work, we have investigated the electronic transport properties of hematite *in situ* under cycling of high quasi-hydrostatic pressures up to ~ 22 GPa. We have established that the original single-crystalline hematite compressed above 5 GPa undergoes a sluggish structural deconfinement, eventually into a nanometric state, with average grain sizes of about ~ 12 – 17 nm. High-pressure behavior of as-prepared bulk nanostructured samples demonstrated a remarkable enhancement of electrical conductivity above 5–7 GPa. Detailed analysis of the thermoelectric power and electrical resistivity data above 5–7 GPa has revealed the pronounced features of two-band electrical conductivity that could be related to the mixed-valence state of the iron ions in nanostructured hematite.

Our findings have some correspondence with a recently revealed dramatic difference in scenarios of pressure-induced magnetic and structural transitions between bulk and nanocrystalline iron;⁴⁷ in the latter, a structural $bcc \rightarrow hcp$ transition shifts to higher pressures, and a state with antiferromagnetic fluctuations is formed as an “intermediate phase.”⁴⁷ Nanocrystalline α -Fe₂O₃ compressed above 5–7 GPa is also expected to exhibit intriguing magnetic and electronic properties. Notice that magnetic and electronic properties of compressed bulk nanostructured samples and deconfined nanoparticles of hematite might differ.

ACKNOWLEDGMENTS

The authors are grateful to L. Dubrovinsky (Bayerisches Geoinstitut [BGI]) for stimulating discussions. The authors are also grateful to H. Keppler (BGI) for assistance in the absorption spectroscopy studies, as well as to D. M.

Trots (BGI) and V. I. Voronin (Institute of Metal Physics) for assistance with the structural analysis. This work was partly supported by Deutsche Forschungsgemeinschaft (DFG; project OV-110/1-1), by the Russian Foundation for Basic

Research (RFBR; project 10-08-00945), by a program of the Russian Academy of Sciences, Urals Division (UD RAS; project 12-P-2-1004), and by the Ministry of Education and Science of the Russian Federation (Contract 14.518.11.7020).

*Corresponding author: sergey.ovsyannikov@uni-bayreuth.de, sergey2503@gmail.com

- ¹B. Lavina, P. Dera, E. Kim, Y. Meng, R. T. Downs, P. F. Weckf, S. R. Sutton, and Y. Zhao, *Proc. Nat. Acad. Sci. USA* **108**, 17281 (2011).
- ²A. J. Bosman and H. J. van Daal, *Adv. Phys.* **19**, 1 (1970); R. F. G. Gardner, F. Sweett, and D. W. Tanner, *J. Phys. Chem. Solids* **24**, 1183 (1963); E. Gartstein, J. B. Cohen, and T. O. Mason, *ibid.* **47**, 775 (1986); C. Gieitzer, J. Nowotny, and M. Rekas, *Appl. Phys. A* **53**, 310 (1991); S. Kerisit and K. M. Rosso, *J. Chem. Phys.* **127**, 124706 (2007); K. M. Rosso, D. M. A. Smith, and M. Dupuis, *ibid.* **118**, 6455 (2003); N. Iordanova, M. Dupuis, and K. M. Rosso, *ibid.* **122**, 144305 (2005); P. Liao, M. C. Toroker, and E. A. Carter, *Nano Lett.* **11**, 1775 (2011).
- ³S. V. Ovsyannikov, V. V. Shchennikov, S. Todo, and Y. Uwatoko, *J. Phys.: Condens. Matter* **20**, 172201 (2008).
- ⁴S. V. Ovsyannikov, V. V. Shchennikov, M. A. Shvetsova, L. S. Dubrovinsky, and A. Polian, *Phys. Rev. B* **81**, 060101 (2010).
- ⁵A. P. Kantor, S. D. Jacobsen, I. Y. Kantor, L. S. Dubrovinsky, C. A. McCammon, H. J. Reichmann, and I. N. Goncharenko, *Phys. Rev. Lett.* **93**, 215502 (2004).
- ⁶G. K. Rozenberg, Y. Amiel, W. M. Xu, M. P. Pasternak, R. Jeanloz, M. Hanfland, and R. D. Taylor, *Phys. Rev. B* **75**, 020102 (2007); Y. Ding, D. Haskel, S. G. Ovchinnikov, Y.-C. Tseng, Y. S. Orlov, J. C. Lang, and H.-K. Mao, *Phys. Rev. Lett.* **100**, 045508 (2008); S. Klotz, G. Steinle-Neumann, Th. Straessle, J. Philippe, Th. Hansen, and M. J. Wenzel, *Phys. Rev. B* **77**, 012411 (2008); N. Su, Y. Han, Y. Ma, H. Liu, B. Ma, and C. Gao, *Appl. Phys. Lett.* **99**, 211902 (2011); K. Glazyrin, C. McCammon, L. Dubrovinsky, M. Merlini, K. Schollenbruch, A. Woodland, and M. Hanfland, *Am. Mineral.* **97**, 128 (2012); J. Ebad-Allah, L. Baldassarre, M. Sing, R. Claessen, V. A. M. Brabers, and C. A. Kuntscher, *High Press. Res.* **29**, 500 (2009); *J. Appl. Phys.* **112**, 073524 (2012); E. R. Morris and Q. Williams, *J. Geophys. Res.* **102**, 18139 (1997); S. A. Gilder, M. LeGoff, J.-C. Chervin, and J. Peyronneau, *Geophys. Res. Lett.* **31**, L10612 (2004).
- ⁷F. P. Koffyberg, K. Dwight, and A. Wold, *Solid State Commun.* **30**, 433 (1979); B. Gilbert, C. Frandsen, E. R. Maxey, and D. M. Sherman, *Phys. Rev. B* **79**, 035108 (2009); A. Fujimori, M. Saeki, N. Kimizuka, M. Taniguchi, and S. Suga, *ibid.* **34**, 7318 (1986).
- ⁸R. R. Rangaraju, A. Panday, K. S. Raja, and M. Misra, *J. Phys. D: Appl. Phys.* **42**, 135303 (2009).
- ⁹A. Kleiman-Shwarstein, M. N. Huda, A. Walsh, Y. Yan, G. D. Stucky, Y.-S. Hu, M. M. Al-Jassim, and E. W. McFarland, *Chem. Mater.* **22**, 510 (2010); F. L. Souza, K. P. Lopes, E. Longo, and E. R. Leite, *Phys. Chem. Chem. Phys.* **11**, 1215 (2009).
- ¹⁰F. J. Morin, *Phys. Rev.* **78**, 819 (1950); **83**, 1005 (1951); **93**, 1195 (1954).
- ¹¹F. Rettig and R. Moos, *Sens. Actuators B* **145**, 685 (2010).
- ¹²G. Rollmann, A. Rohrbach, P. Entel, and J. Hafner, *Phys. Rev. B* **69**, 165107 (2004); J. R. Morales, J. E. Garay, M. Biasini, and W. P. Beyermann, *Appl. Phys. Lett.* **93**, 022511 (2008).
- ¹³R. C. Liebermann and K. A. Maasch, *J. Geophys. Res.* **91**, 4651 (1986); R. C. Liebermann and S. K. Banerjee, *J. Appl. Phys.* **41**, 1414 (1970).
- ¹⁴G. K. Lewis, Jr. and H. G. Drickamer, *J. Chem. Phys.* **45**, 224 (1966); Y. Sato and S. Akimoto, *J. Appl. Phys.* **50**, 5285 (1979).
- ¹⁵J. Muench, S. Araj, and E. Matijevic, *Phys. Status Solidi A* **92**, 187 (1985); O. Oezdemir, D. J. Dunlop, and T. S. Berquo, *Geochem. Geophys. Geosyst.* **9**, Q10Z01 (2008); R. D. Zysler, D. Fiorani, A. M. Testa, L. Suber, E. Agostinelli, and M. Godinho, *Phys. Rev. B* **68**, 212408 (2003).
- ¹⁶D. L. Williamson, E. L. Venturini, R. A. Graham, and B. Morosin, *Phys. Rev. B* **34**, 1899 (1986).
- ¹⁷S. Mitra, S. Das, S. Basu, P. Sahu, and K. Mandal, *J. Magn. Magn. Mater.* **321**, 2925 (2009).
- ¹⁸Y. F. Krupyanskii and I. P. Suzdalev, *Sov. Phys. JETP* **38**, 859 (1974).
- ¹⁹T. G. Worlton, R. B. Bennion, and R. M. Brugger, *Phys. Lett. A* **24**, 653 (1967); J. B. Parise, D. R. Locke, C. A. Tulk, I. Swainson, and L. Cranswick, *Physica B* **385-386**, 391 (2006).
- ²⁰I. N. Goncharenko, J.-M. Mignot, G. Andre, O. A. Lavrova, I. Mirebeau, and V. A. Somenkov, *High Press. Res.* **14**, 41 (1995).
- ²¹R. W. Vaughan and H. G. Drickamer, *J. Chem. Phys.* **47**, 1530 (1967); Y. Syono, A. Ito, S. Morimoto, T. Suzuki, T. Yagi, and S. Akimoto, *Solid State Commun.* **50**, 97 (1984).
- ²²T. Kawakami, S. Nasu, T. Tsutsui, T. Sasaki, T. Yamada, S. Endo, M. Takano, and T. Katamoto, *J. Phys. Soc. Jpn.* **72**, 2640 (2003); G. Hearne and V. Pischedda, *J. Solid State Chem.* **187**, 134 (2012).
- ²³S. Klotz, K. Takemura, Th. Strässle, and Th. Hansen, *J. Phys.: Condens. Matter* **24**, 325103 (2012).
- ²⁴N. Kawai and S. Mochizuki, *Phys. Lett. A* **36**, 54 (1971); K. Kondo, T. Sunakawa, and A. Sawaoka, *Jpn. J. Appl. Phys.* **18**, 851 (1979); E. Knittle and R. Jeanloz, *Solid State Commun.* **58**, 129 (1986); M. P. Pasternak, G. Kh. Rozenberg, G. Yu. Machavariani, O. Naaman, R. D. Taylor, and R. Jeanloz, *Phys. Rev. Lett.* **82**, 4663 (1999).
- ²⁵V. V. Shchennikov, S. V. Ovsyannikov, A. E. Karkin, S. Todo, and Y. Uwatoko, *Solid State Commun.* **149**, 759 (2009).
- ²⁶V. V. Shchennikov, S. V. Ovsyannikov, and A. V. Bazhenov, *J. Phys. Chem. Solids* **69**, 2315 (2008); V. V. Shchennikov, S. V. Ovsyannikov, and A. Y. Manakov, *ibid.* **71**, 1168 (2010).
- ²⁷S. V. Ovsyannikov and V. V. Shchennikov, *Appl. Phys. Lett.* **90**, 122103 (2007); S. V. Ovsyannikov, V. V. Shchennikov, A. E. Karkin, A. Polian, O. Briot, S. Ruffenach, B. Gil, and M. Moret, *ibid.* **97**, 032105 (2010); V. V. Shchennikov, N. V. Morozova,

- I. Tyagur, Y. Tyagur and S. V. Ovsyannikov, *ibid.* **99**, 212104 (2011); S. V. Ovsyannikov, I. V. Korobeinikov, N. V. Morozova, A. Misiuk, N. V. Abrosimov, and V. V. Shchennikov, *ibid.* **101**, 062107 (2012).
- ²⁸K. Seeger, *Semiconductor Physics* (Springer-Verlag, Wien-N.Y., 1973).
- ²⁹S. V. Ovsyannikov, V. V. Shchennikov, G. V. Vorontsov, A. Y. Manakov, A. Y. Likhacheva, and V. A. Kulbachinskii, *J. Appl. Phys.* **104**, 053713 (2008); V. V. Shchennikov, N. V. Morozova, and S. V. Ovsyannikov, *ibid.* **111**, 112624 (2012).
- ³⁰S. V. Ovsyannikov, X. Wu, V. V. Shchennikov, A. E. Karkin, N. Dubrovinskaya, G. Garbarino, and L. Dubrovinsky, *J. Phys.: Condens. Matter* **22**, 375402 (2010).
- ³¹S. K. Patapis, *Solid State Commun.* **52**, 925 (1984).
- ³²G. K. Williamson and W. H. Hall, *Acta Metall.* **1**, 22 (1953).
- ³³D. Chrobak, N. Tymiak, A. Beaber, O. Ugurlu, W. W. Gerberich, and R. Nowak, *Nat. Nanotech.* **6**, 480 (2011).
- ³⁴L. W. Finger and R. M. Hazen, *J. Appl. Phys.* **51**, 5362 (1980).
- ³⁵P. Schouwink, L. Dubrovinsky, K. Glazyrin, M. Merlini, M. Hanfland, T. Pippinger, and R. Miletich, *Am. Mineral.* **96**, 1781 (2011).
- ³⁶S.-H. Shim and T. S. Duffy, *Am. Mineral.* **87**, 318 (2001); J. Badro, G. Fiquet, V. V. Struzhkin, M. Somayazulu, H.-K. Mao, G. Shen, and T. Le Bihan, *Phys. Rev. Lett.* **89**, 205504 (2002); G. Kh. Rozenberg, L. S. Dubrovinsky, M. P. Pasternak, O. Naaman, T. Le Bihan, and R. Ahuja, *Phys. Rev. B* **65**, 064112 (2002); S. Ono, T. Kikegawa, and Y. Ohishi, *J. Phys. Chem. Solids* **65**, 1527 (2004); S. Ono and Y. Ohishi, *ibid.* **66**, 1714 (2005); E. Ito, H. Fukui, T. Katsura, D. Yamazaki, T. Yoshino, Y. Aizawa, A. Kubo, S. Yokoshi, K. Kawabe, S. Zhai, A. Shatzkiy, M. Okube, A. Nozawa, and K. Funakoshi, *Am. Mineral.* **94**, 205 (2009); J. Staun Olsen, C. S. G. Cousins, L. Gerward, H. Jhans, and B. J. Sheldon, *Phys. Scr.* **43**, 327 (1991); L. Machala, J. Tuček, and R. Zbořil, *Chem. Mater.* **23**, 3255 (2011); J.-F. Lin, J. S. Tse, E. E. Alp, J. Zhao, M. Lerche, W. Sturhahn, Y. Xiao, and P. Chow, *Phys. Rev. B* **84**, 064424 (2011); Z. Wang and S. K. Saxena, *Solid State Commun.* **123**, 195 (2002); N. C. Wilson and S. P. Russo, *Phys. Rev. B* **79**, 094113 (2009).
- ³⁷P. Perlin, C. Jauberthie-Carillon, J.-P. Itie, A. San Miguel, I. Grzegory, and A. Polian, *Phys. Rev. B* **45**, 83 (1992).
- ³⁸H. Liu, W. A. Caldwell, L. R. Benedetti, W. Panero, and R. Jeanloz, *Phys. Chem. Miner.* **30**, 582 (2003).
- ³⁹J. Z. Jiang, J. Staun Olsen, L. Gerward, and S. Morup, *Europhys. Lett.* **44**, 620 (1998); S. M. Clark, S. G. Prilliman, C. K. Erdonmez, and A. P. Alivisatos, *Nanotechnology* **16**, 2813 (2005); H. Zhu, Y. Ma, H. Yang, C. Ji, D. Hou, and L. Guo, *J. Phys. Chem. Solids* **71**, 1183 (2010).
- ⁴⁰G. Patermarakis, J. Papaioannou, H. Karayianni, and K. Masavetas, *J. Electrochem. Soc.* **151**, J62 (2004), and references therein.
- ⁴¹F. Rodolakis, P. Hansmann, J.-P. Rueff, A. Toschi, M. W. Haverkort, G. Sangiovanni, A. Tanaka, T. Saha-Dasgupta, O. K. Andersen, K. Held, M. Sikora, I. Alliot, J.-P. Itie, F. Baudelet, P. Wzietek, P. Metcalf, and M. Marsi, *Phys. Rev. Lett.* **104**, 047401 (2010); S. V. Ovsyannikov, X. Wu, A. E. Karkin, V. V. Shchennikov, and G. M. Manthilake, *Phys. Rev. B* **86**, 024106 (2012).
- ⁴²F. Bodker, M. F. Hansen, C. B. Koch, K. Lefmann, and S. Morup, *Phys. Rev. B* **61**, 6826 (2000).
- ⁴³M. V. Sahana, C. Sudakar, G. Setzler, A. Dixit, J. S. Thakur, G. Lawes, R. Naik, V. M. Naik, and P. P. Vaishnava, *Appl. Phys. Lett.* **93**, 231909 (2008); H. M. Fan, G. J. You, Y. Li, Z. Zheng, H. R. Tan, Z. X. Shen, S. H. Tang, and Y. P. Feng, *J. Phys. Chem. C* **113**, 9928 (2009); L. Chen, X. Yang, J. Chen, J. Liu, H. Wu, H. Zhan, C. Liang, and M. Wu, *Inorg. Chem.* **49**, 8411 (2010).
- ⁴⁴T. Kawakami and S. Nasu, *J. Phys.: Condens. Matter* **17**, S789 (2005).
- ⁴⁵M. S. Senn, J. P. Wright, and J. P. Attfield, *Nature* **481**, 173 (2012).
- ⁴⁶D. M. Zhang, Y. S. Zhang, Y. Gao, Y. H. Han, C. X. Gao, Y. Z. Ma, C. X. Cheng, and K. Yu, *J. Appl. Phys.* **111**, 063718 (2012).
- ⁴⁷A. Monza, A. Meffre, F. Baudelet, J.-P. Rueff, M. d'Astuto, P. Munsch, S. Huotari, S. Lachaize, B. Chaudret, and A. Shukla, *Phys. Rev. Lett.* **106**, 247201 (2011).